Article

Current Biology

Autoregulation of *RCO* by Low-Affinity Binding Modulates Cytokinin Action and Shapes Leaf Diversity

Graphical Abstract

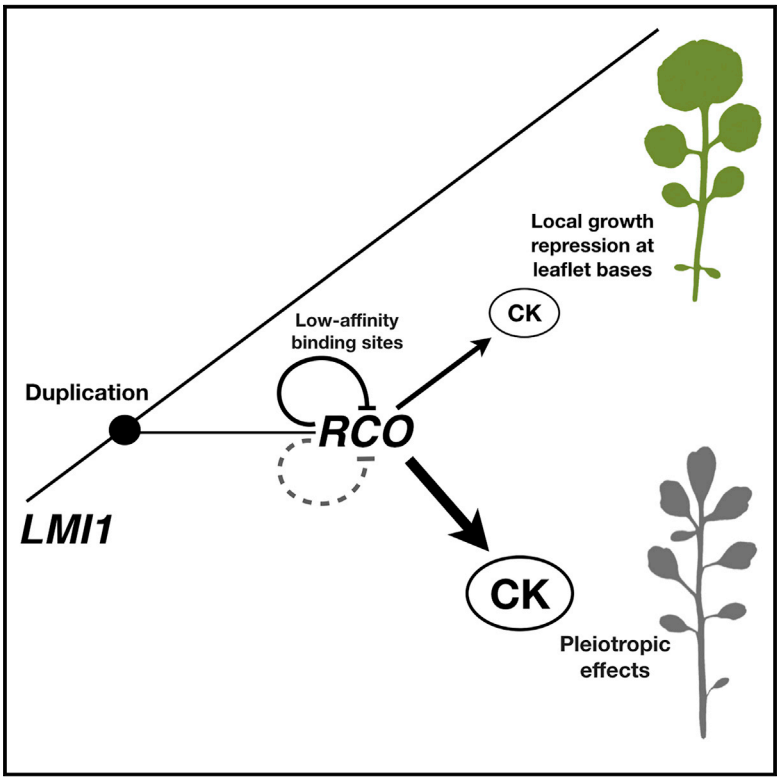

Authors

Mohsen Hajheidari, Yi Wang, Neha Bhatia, ..., Peter Huijser, Xiangchao Gan, Miltos Tsiantis

Correspondence

tsiantis@mpipz.mpg.de

In Brief

Hajheidari et al. identify target genes for the RCO homeodomain protein that drove leaf shape diversity. They show that RCO regulates growth via orchestrating homeostasis for the hormone cytokinin and that it also represses its own transcription via low-affinity binding sites. This autorepression helps delimit *RCO* expression and shape leaf form.

Highlights

- Identification of genome-wide target genes for the RCO transcription factor
- RCO delimits its own expression through autorepression by low-affinity binding
- RCO represses local leaf growth via regulating multiple cytokinin (CK)-related genes
- RCO negative autorepression fine-tunes CK activity and regulates leaf shape

Hajheidari et al., 2019, Current Biology *29*, 4183–4192
December 16, 2019
https://doi.org/10.1016/j.cub.2019.10.040

CellPress

Current Biology
Article

Autoregulation of *RCO* by Low-Affinity Binding Modulates Cytokinin Action and Shapes Leaf Diversity

Mohsen Hajheidari,[1,6] Yi Wang,[1] Neha Bhatia,[1] Francesco Vuolo,[1,7] José Manuel Franco-Zorrilla,[2] Michal Karady,[4,10] Remco A. Mentink,[1,8] Anhui Wu,[1,9] Bello Rilwan Oluwatobi,[1] Bruno Müller,[5] Raffaele Dello Ioio,[3] Stefan Laurent,[1] Karin Ljung,[4] Peter Huijser,[1] Xiangchao Gan,[1] and Miltos Tsiantis[1,11,*]

[1]Department of Comparative Development and Genetics, Max Planck Institute for Plant Breeding Research, Carl-von-Linné-Weg 10, 50829 Cologne, Germany

[2]Unidad de Genómica and Departamento de Genética Molecular de Plantas, Centro Nacional de Biotecnología–Consejo Superior de Investigaciones Científicas, Calle Darwin 3, 28049 Madrid, Spain

[3]Department of Biology and Biotechnology, Laboratory of Functional Genomics and Proteomics of Model Systems, Sapienza University of Rome, Via dei Sardi 70, 00185 Rome, Italy

[4]Umeå Plant Science Centre, Department of Forest Genetics and Plant Physiology, Swedish University of Agricultural Sciences, 901 83 Umeå, Sweden

[5]Leibniz Institute of Plant Genetics and Crop Plant Research, Correnstr. 3, 06466 Seeland, Gatersleben, Germany

[6]Present address: Botanical Institute, Cologne Biocenter, University of Cologne, 50674 Cologne, Germany

[7]Present address: Sacco srl, Via Alessandro Manzoni 29/A, 22071 Cadorago, CO, Italy

[8]Present address: Bejo Zaden B.V., Trambaan 1, 1749 Warmenhuizen, the Netherlands

[9]Present address: Institute of Plant Sciences, University of Bern, Altenbergrain 21, 3013 Bern, Switzerland

[10]Present address: Department of Chemical Biology and Genetics, Centre of the Region Hana for Biotechnological and Agricultural Research, Faculty of Science, Palacky University, 783 71 Olomouc, Czech Republic

[11]Lead Contact

*Correspondence: tsiantis@mpipz.mpg.de

https://doi.org/10.1016/j.cub.2019.10.040

SUMMARY

Mechanisms through which the evolution of gene regulation causes morphological diversity are largely unclear. The tremendous shape variation among plant leaves offers attractive opportunities to address this question. In cruciferous plants, the REDUCED COMPLEXITY (RCO) homeodomain protein evolved via gene duplication and acquired a novel expression domain that contributed to leaf shape diversity. However, the molecular pathways through which RCO regulates leaf growth are unknown. A key question is to identify genome-wide transcriptional targets of RCO and the DNA sequences to which RCO binds. We investigate this question using *Cardamine hirsuta*, which has complex leaves, and its relative *Arabidopsis thaliana*, which evolved simple leaves through loss of *RCO*. We demonstrate that RCO directly regulates genes controlling homeostasis of the hormone cytokinin to repress growth at the leaf base. Elevating cytokinin signaling in the *RCO* expression domain is sufficient to both transform *A. thaliana* simple leaves into complex ones and partially bypass the requirement for *RCO* in *C. hirsuta* complex leaf development. We also identify *RCO* as its own target gene. RCO directly represses its own transcription via an array of low-affinity binding sites, which evolved after *RCO* duplicated from its progenitor sequence. This autorepression is required to limit *RCO* expression. Thus, evolution of low-affinity binding sites created a negative autoregulatory loop that facilitated leaf shape evolution by defining *RCO* expression and fine-tuning cytokinin activity. In summary, we identify a transcriptional mechanism through which conflicts between novelty and pleiotropy are resolved during evolution and lead to morphological differences between species.

INTRODUCTION

cis-regulatory variation of developmental genes plays a pivotal role in morphological evolution of plants and animals and often involves diversification of transcriptional enhancers [1–8]. Regulatory sequence variation is believed to facilitate morphological change while minimizing the potentially adverse effects of pleiotropy—the phenomenon by which a single gene influences multiple aspects of development [1, 9, 10]. However, the precise mechanisms that link *cis*-regulatory changes to morphological diversity remain poorly understood [11, 12]. For example, do *cis*-regulatory changes at transcription factor loci cause specific effects on downstream gene expression or global transcriptome remodeling? Do these transcriptional changes affect few genes with large effects on development or a multitude of downstream processes with small effect? And how do *cis*-regulatory changes circumvent pleiotropy, given that transcriptional enhancers can show considerable pleiotropy despite their modularity [13]?

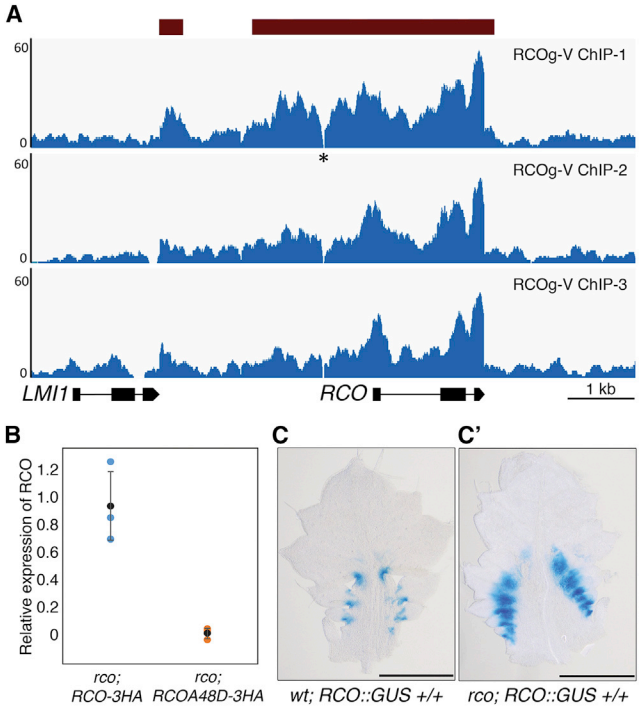

Figure 1. Genome-wide Analysis of RCO-Binding Peaks in *C. hirsuta* Reveals *RCO* Autoregulation

(A) *RCO* ChIP-seq profile (blue) along the *RCO* locus in three biological replicates. Numbers on the y axis represent read coverage. Brown-filled rectangles indicate the peak regions of RCO binding from MACS2 [21]. The asterisk indicates the un-mapped gap regions.

(B) qRT-PCR comparing *RCO* and *RCOA48D* transcript levels in seedlings. Black dots depict the mean of three biological replicates of qRT-PCR, each in three independent lines expressing *RCO-3HA* and *RCOA48D-3HA*. Blue and orange dots represent individual data points. Error bars represent ± 1 SD.

(C and C′) Light microscopy images of GUS staining in leaves showing the expression of *pRCO::GUS* in *C. hirsuta* wild-type (WT) (*Oxford*; C) and *rco* mutant (C′) carrying a single copy of the *pRCO::GUS* transgene. Note an increased GUS staining signal in the leaves of *rco* mutants relative to WT plants. Scale bars, 500 μm (C and C′).

See also Figure S1 and Data S1A.

Recent work indicates that low-affinity transcription factor binding sites play a vital role in fine-tuning developmental gene expression, thus ensuring its specificity and robustness [14]. These sites can evolve rapidly and therefore might also have important yet undiscovered roles in morphological evolution [15].

Plant leaves provide a powerful model in which to explore such questions on the mechanistic basis of evolutionary change because they show substantial, heritable morphological variation at different evolutionary scales and are ecophysiologically important because they fix CO_2 in terrestrial ecosystems [16, 17]. Considerable insights into the genetic basis for diversification of leaf shape have come from comparative studies of simple leaves of the reference plant *A. thaliana* versus complex leaves of its relative *Cardamine hirsuta*, where leaves are divided into distinct units called leaflets. The *RCO* gene was discovered in *C. hirsuta* on the basis of its simplified mutant phenotype, and *RCO*-type genes support development of leaf marginal outgrowths of different sizes in different crucifer species. *RCO* arose by duplication of its ancestral paralog *LATE MERISTEM IDENTITY 1* (*LMI1*), which is conserved in seed plants, and its emergence promoted evolution of leaf complexity in crucifers [18]. Neofunctionalization of an *RCO* enhancer element (*RCO*^{enh500}) altered leaf shape by changing *RCO* expression from the distal leaf blade to the leaf base [19]. In this domain, *RCO* represses growth in a series of foci along the leaf margin, allowing the outgrowth of lobes or leaflets between flanking regions of *RCO* expression [20]. *RCO* was secondarily lost from the *A. thaliana* genome, leading to leaf simplification. However, its reintroduction in *A. thaliana* as a transgene was sufficient to increase leaf complexity, demonstrating that *RCO* is a large-effect gene underlying morphological evolution. However, the downstream effector genes through which RCO acts to repress growth and the upstream transcriptional inputs that delimit *RCO* expression are both unknown.

To address these issues, we identified genome-wide RCO target genes by combining chromatin immunoprecipitation sequencing (ChIP-seq) and RNA sequencing (RNA-seq) experiments. We further conducted functional validation of our findings using genetics, molecular biology, microscopy, and hormone measurements. In this way, we show that RCO coordinates homeostasis of the hormone cytokinin (CK) through direct regulation of multiple genes involved in CK biosynthesis and catabolism and provide evidence that this RCO/CK module is required for complex leaf development. In parallel, we show that RCO directly delimits its own expression through binding to clusters of low-affinity repressive sites in its 5′ upstream regulatory region and gene body and that this autoregulatory loop also shapes CK activity in the leaf. Thus, a paradigm emerges whereby low-affinity binding sites facilitated morphological evolution by dampening the effects of *cis*-regulatory divergence in a potent transcription factor. We propose that this regulatory architecture allowed regulatory evolution to fine-tune levels of hormonal homeostasis and circumvent pleiotropy.

RESULTS AND DISCUSSION

Genome-wide Identification of Molecular Targets of RCO Reveals It Is Subject to Negative Autoregulation

To understand the molecular basis of RCO's action in *C. hirsuta*, we performed ChIP-seq profiling in three biological replicates of *C. hirsuta rco* mutant plants expressing *pRCO::RCOgenomic-VENUS* using an anti-GFP antibody (see STAR Methods for details). We identified 598 binding peaks for 592 potential target genes, which showed a consistent binding pattern across all biological replicates (Data S1A). *RCO* is among the top 10 potential target genes of RCO, according to ranking of peaks by p value, and RCO associates with chromatin at its own promoter and gene body in a single broad peak (Figures 1A and S1; Data S1A). By contrast, a single narrow peak was detected at the 3′ end of *LMI1*—the ancestral paralog of *RCO* (Figures 1A and S1; Data S1A). To test whether RCO regulates its own expression, we compared *RCO* expression in transgenic *rco* mutant lines complemented with either the native version of RCO or the stabilized form of RCO (RCOA48D) [19]. In the RCOA48D lines where protein levels are elevated relative to native RCO [19], we found reduced *RCO* transcript levels compared to *rco* mutant lines expressing the native *RCO* gene

(Figure 1B). This indicates that *RCO* might undergo negative autoregulation, an idea further supported by the observation that a single-copy *RCO::GUS* reporter gene showed broader and stronger expression in *rco* leaves compared to wild type (Figures 1C and 1C′). Together, these results suggest that RCO represses its own expression.

Negative Autoregulation of *RCO* Requires Low-Affinity Binding Sites to Delimit *RCO* Expression and Regulate Leaf Shape

If RCO binds to the *RCO* locus to negatively regulate its own expression, then deletion or randomization of these binding sites should increase *RCO* expression. To test this prediction, we selected 4 binding candidate fragments (BCFs): three fragments with the highest read coverage in the promoter region and the first intron and another fragment covering the whole second intron (Figure S2A). We engineered *RCO* promoter fragments in which the BCF1 and BCF2 were deleted, randomized, or replaced by the corresponding *LMI1* sequence, where RCO is not expected to bind. Each modified *RCO* promoter was fused to both *RCO*-coding sequence (*RCO-CDS*) lacking BCF3 and BCF4 and the genomic sequence (including BCF3 and BCF4), including introns that harbor RCO-binding sites (*RCOgenomic*), from the ATG-start to the stop codon (Figures S2A and S2G). All constructs, including controls bearing the native promoter sequence, were transformed into the *rco* mutant background. We observed that removing peaks or modifying them, as described above, increased *RCO* expression (Figure S2C). In *rco* mutant plants containing the modified *RCO* promoters fused to *RCO-CDS*, which caused higher *RCO* expression, leaf shape was significantly altered—leaf dissection increased while leaf area and seed mass decreased (Figures S2B–S2F). Notably, transgenic *rco* mutant plants that expressed *RCOgenomic* (ATG-stop) driven by modified *RCO* promoters produced either wild-type or partially rescued leaves (Figures S2G and S2H). This indicates that deleting or modifying BCFs 1 and 2 within the *RCO* promoter sequence is insufficient to alter leaf development if BCFs 3 and 4 are still present in the gene body. Nevertheless, these constructs still rescued the *rco* mutant phenotype more effectively than the control construct (Figures S2G and S2H). In summary, RCO autorepression depends on multiple sites in its genomic locus and perturbing this autorepression has detrimental effects on leaf development and plant performance.

We next sought to understand the *cis*-regulatory logic that underlies *RCO* autorepression. We first used protein-binding microarrays (PBMs) to identify the DNA-binding motifs that RCO binds to with high affinity *in vitro* (Figure S3A; Data S1B). We then constructed position weight matrices (PWMs) using these sequences, which we refer to as canonical binding sites [22]. However, when we scanned the peak sequences at the *RCO* locus with the PBM-derived PWMs using FIMO (default settings), we did not find canonical RCO-binding sites [23, 24]. Yet we found canonical sites in 64 of the genome-wide identified RCO-binding peaks. These observations suggest that RCO-DNA binding may be influenced by protein interactions and/or the chromatin context, as is the case for other transcription factors [25–27]. To identify RCO-binding sites within the *RCO* locus, we used electrophoretic mobility shift assays (EMSAs) with native and mutagenized oligonucleotides to screen the four BCFs selected previously. In this way, we identified 11 RCO-binding sites residing on nine 55-bp fragments (Figure 2). These sites are AT-rich, a feature shared with both the canonical binding sites identified in the PBM and a motif enriched in RCO-bound ChIP-seq peaks (Figures 2A, 2B, S3B, and S3C; Data S1B). These 11 RCO-binding sites in the *RCO* locus showed concentration-dependent binding to RCO (Figures 2A and 2B) with 2 of the 11 sites located within RCO^{enh500} (Figures 2A and S4A). All the 11 binding sites show considerable conservation in crucifers (Figure S4B). Statistical analysis (STAR Methods) indicated that evolution of an array of low-affinity, but not high-affinity, binding sites in *RCO* is unlikely to reflect chance ($P_{neut}(X = 0) = 0.024$, where P_{neut} is the probability of observing X high-affinity binding sites under a neutral evolutionary model for the *RCO/LMI1* duplication). In turn, this suggests that selective processes likely prevented accumulation of high-affinity binding sites in *RCO* while permitting emergence of low-affinity ones. Overall, these findings suggest that RCO^{enh500} co-evolved with an array of low-affinity RCO-binding sites to provide specificity to *RCO* expression via negative autoregulation.

To test this hypothesis and understand the mechanism of action of these native RCO-binding sites, we compared their binding affinity to that of the canonical RCO binding sites defined by PBMs. We did this by performing EMSAs with native oligonucleotide sequences and oligos containing the canonical binding site (CAATAATT). Oligos with the native sites were outcompeted and failed to bind to RCO in the presence of an equal amount of oligos containing the canonical binding sites, indicating that native sites bind to RCO with a lower affinity than does the canonical RCO-binding site (Figures 2C and S3D). We thus hypothesized that these low-affinity native binding sites may play a crucial role in shaping the distinctive expression pattern of *RCO* around emerging leaflets. To test this idea, we made an *RCOg* construct that contains the high-affinity canonical binding sites in place of the native sites and introduced it into the *rco* mutant. This construct could not rescue the *rco* mutant phenotype, likely due to low levels of *RCO* expression reflecting autorepression (Figure S3E). To assay the functionality of low-affinity RCO-binding sites *in vivo*, we engineered an *RCO* promoter fragment in which the low-affinity binding sites were mutagenized (termed *pmutRCO*). This mutagenized promoter was then used to drive the expression of *RCOgenomic-VENUS* (*pmutRCO::RCOg-VENUS*) and *RCOcds-VENUS* (*pmutRCO::RCOcds-VENUS*) (Figure 3A). The resulting constructs and the control constructs comprising the native, non-mutagenized *RCO* promoter fused to *RCOgenomic-VENUS* (*pRCO::RCOg-VENUS*) and *RCOcds-VENUS* (*pRCO::RCOcds-VENUS*) were transformed into the *rco* mutant. In transgenic plants expressing *pmutRCO::RCOcds-VENUS* (no RCO-binding sites), RCO-VENUS levels and leaf complexity were significantly increased, relative to transgenic plants that contain either the native construct *pRCO::RCOg-VENUS*, which has all the RCO-binding sites, or the *pmutRCO::RCOg-VENUS* construct, which also includes the introns and consequently additional RCO-binding sites (Figures 3B–3E). In addition, ectopic *RCO* expression was detectable at the boundaries of terminal leaflets in *pmutRCO::RCOcds-VENUS*-expressing transgenic plants (white arrow in Figure 3E). *RCO* expression was also higher in *rco* mutant lines expressing *pmutRCO::RCOg-VENUS* than in *rco* mutant plants

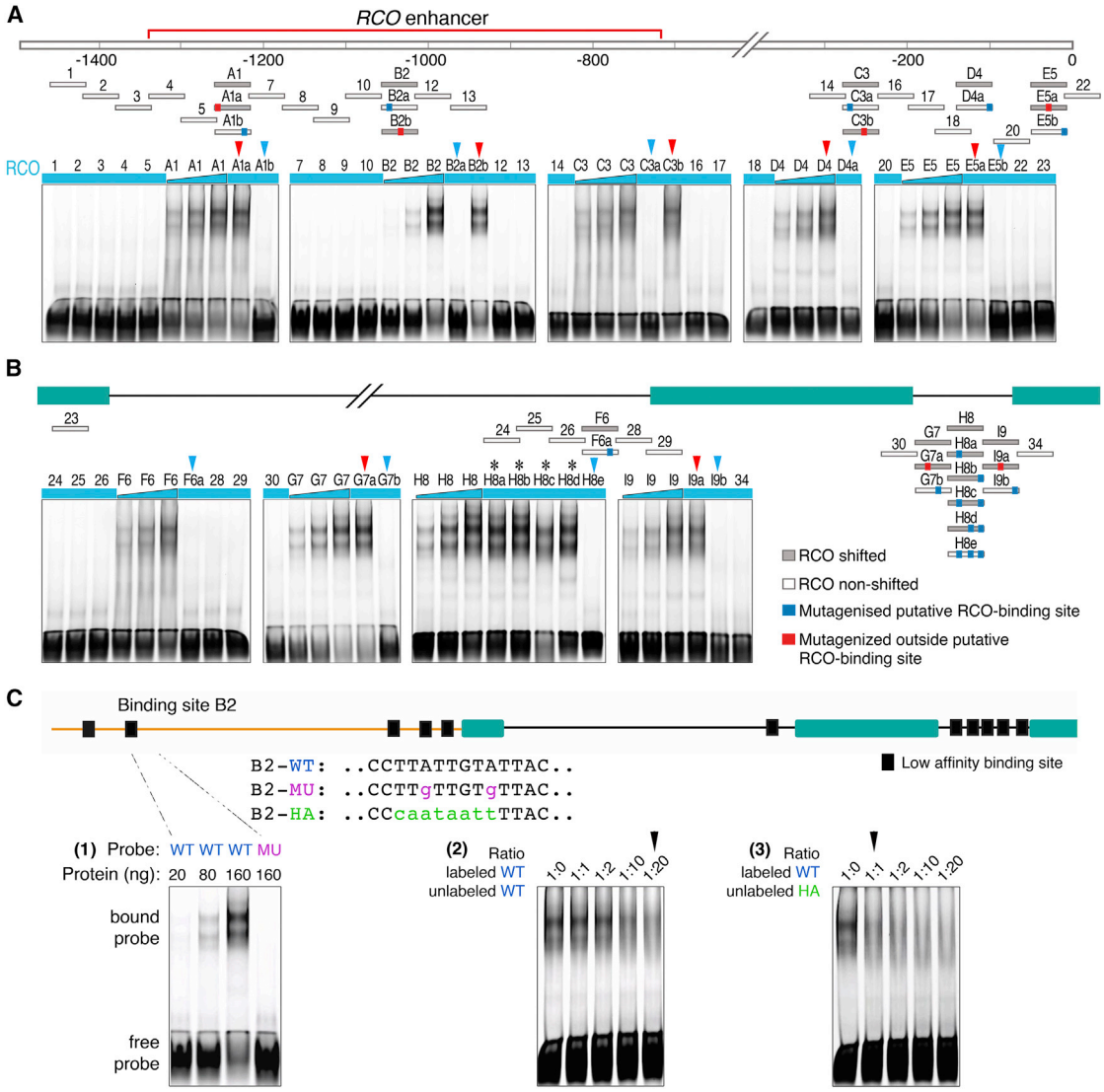

Figure 2. RCO Regulates Its Own Expression through Binding to Clusters of Low-Affinity Binding Sites

(A and B) Schematic representation of the *RCO* promoter features (A) and *RCO* gene body features (B) showing introns (black lines) and exon (green boxes) regions. The labeled bars under the schematics represent the oligos with corresponding DNA sequences that were tested for their ability to bind with the RCO protein in EMSA. Numbered white bars (1–5, 7–10, 12–14, 16–18, 20, 22–26, 28 to 29, 30, and 34) represent oligos to which RCO did not bind (RCO non-shifted, EMSA gel images). Labeled gray bars (A1 to I9) represent oligos bound by RCO (RCO shifted, EMSA gel images). The small blue and red boxes on the bars represent the mutagenesis of 2 to 3 T nucleotides to G nucleotides in the AT-rich clusters within the putative RCO binding sites (blue) or outside the putative RCO binding sites (red boxes; see Table S3 for oligos). The mutations within the putative RCO-binding sites could suppress the RCO binding (no shifts in the gel, blue arrowheads), but mutations outside the putative RCO-binding sites did not suppress RCO binding (red arrowheads). Note that, for oligo position H8, there were three putative RCO-binding sites and binding was inhibited only upon mutagenizing all the three sites (asterisks and blue arrowhead in B). The thickness of turquoise bars above each gel image represents RCO protein concentration in the increments of 20 (minimum thickness), 80, and 160 ng (maximum thickness).
(C) EMSA showing the low-affinity binding behavior of RCO using the binding site B2 as an example (also shown in Figure S3). Top: schematic representation of *pRCO::RCOg* construct; promoter (orange line), exon (green boxes), intron (black line), and low-affinity RCO binding sites (black boxes). Middle: core sequences of the oligos used for EMSA with WT binding sequences (B2-WT; the same as B2 in A), mutated binding sequences (B2-MU; marked in magenta, the same as B2a in A), and binding sequences replaced with the canonical sequence (CAATAATT in B2-HA; marked in green).
(C1) EMSA showing the binding of RCO to B2-WT and not to B2-MU.
(C2 and C3) Competition test with B2-WT (C1) and B2-HA (C2) oligos. A constant amount of *in vitro* synthesized RCO protein and IRDye-800-labeled B2-WT oligos were mixed with unlabeled B2-WT or unlabeled B2-HA oligos. Note that 20x concentration of unlabeled B2-WT reduced the binding of labeled WT oligos, while 1x concentration of unlabeled B2-HA oligos was sufficient to reduce the binding of labeled WT oligos (compare lanes marked by black arrowheads in C2 and C3).
See also Figures S2–S4 and Data S1B.

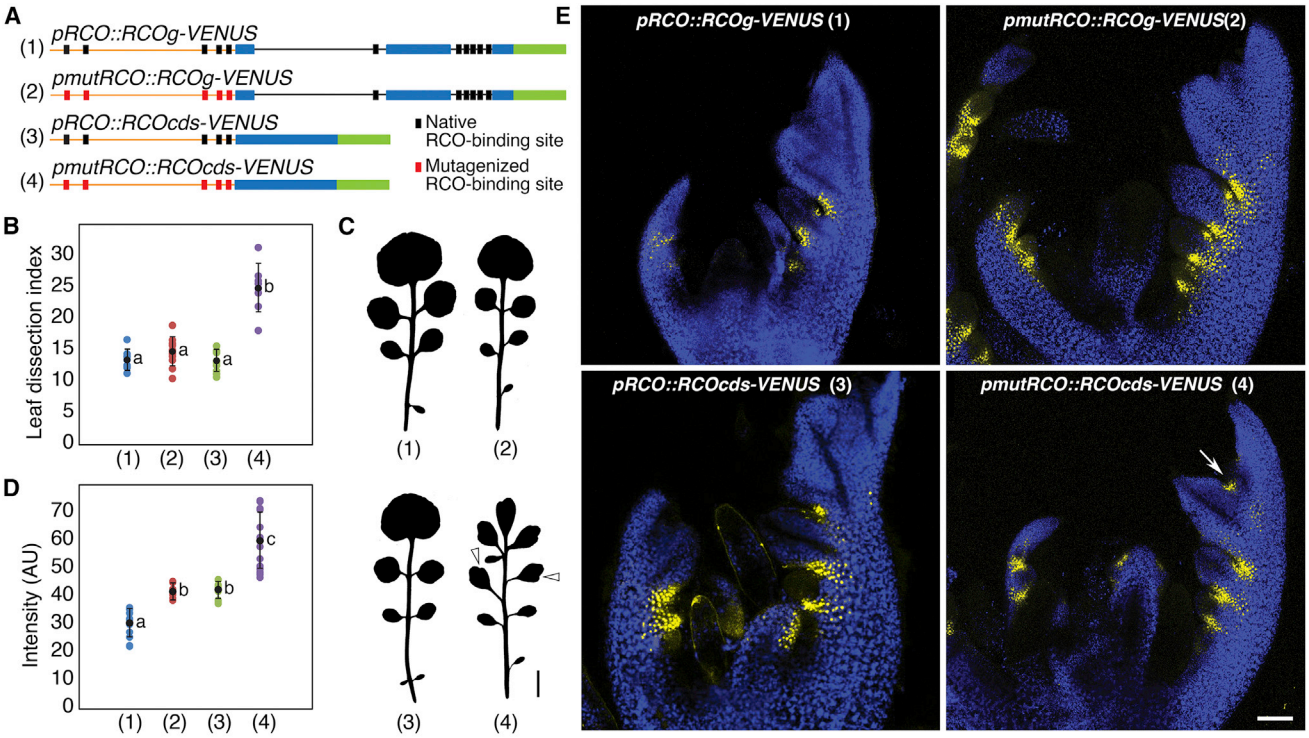

Figure 3. Low-Affinity Binding Sites Help Define the Domain and Level of *RCO* Gene Expression

(A) Schematic representation of the WT constructs and constructs engineered for introducing mutations in the RCO-binding sites within the promoter regions driving either the *RCO* genomic sequence or the coding sequence (CDS). Orange lines represent the *RCO* promoter, and the black lines represent the introns. Blue boxes represent either exons or the *RCO* CDS. Green boxes represent *VENUS* fluorescent protein sequence. Native RCO binding sites and the sites engineered for mutagenesis are indicated in black and red, respectively. All the constructs were transformed into the *rco* mutant background

(B) Leaf dissection index of *rco* mutant lines expressing the constructs described in (A). The numbers (1–4) on x axis correspond to the constructs shown in (A). Black dots indicate the means of 8 independent T1 lines of *rco* expressing *pRCO::RCOg-VENUS* (1), 11 independent T1 lines of *rco* expressing *pmutRCO::RCOg-VENUS* (2), 9 independent T1 lines of *rco* expressing *pRCO::RCOcds-VENUS* (3), and 8 independent T1 lines of *rco* expressing *pmutRCO::RCOcds-VENUS* (4). Error bars indicate ± 1 SD. Note a higher leaf dissection index corresponding to increased complexity in the leaves of *rco* mutant plants expressing *RCO* lacking autoregulation (*pmutRCO::RCOcds-VENUS*).

(C) Representative silhouettes of leaf 5 of *rco* transgenic lines harboring constructs shown in (A). Note a further subdivision of the terminal leaflet as well as increased complexity in the lateral leaflets (lobes pointed by arrowheads in [4] upon inhibiting *RCO* autoregulation).

(D) Quantifications of VENUS fluorescence intensity in *rco* mutant lines expressing constructs shown in (A). AU indicates arbitrary units of fluorescence intensity normalized to area. Black dots indicate means of 9–15 independent measurements from at least seven independent T1 lines for each construct. Note increased intensity of RCO-VENUS lacking autoregulation. Error bars indicate ± 1 SD.

(E) Representative confocal projections showing expression patterns of RCO-VENUS (yellow) in the different constructs shown in (A) within the young leaves of *rco* mutants (n = 10(E1); n = 8(E2); n = 11(E3); n = 12(E4)). Autofluorescence is shown in (blue). Note the extended expression of RCO-VENUS at sinuses in between the terminal leaflet in *pmutRCO::RCOcds-VENUS* (white arrow in E4), which contains no binding sites for RCO, thereby lacking autoregulation.

Significance groups are determined based on Tukey's HSD test for multiple pairwise comparisons in (B) and (D). Only pairwise comparisons involving different groups, labeled a–c (B and D), are significant at the 5% level. Scale bars, 1 cm (C) and 50 μm (E).

expressing the *pRCO::RCOg-VENUS* construct (compare RCO-VENUS fluorescence in [1] and [2] in Figures 3D and 3E). However, we did not observe a significant difference in their leaf complexity (compare [1] and [2] in Figures 3B and 3C). Our results demonstrate that low-affinity RCO-binding sites act redundantly with each other to shape leaf development by defining the correct *RCO* gene expression pattern and dose, thereby preventing pleiotropic RCO effects.

RCO Directly Regulates Genes Involved in CK Biosynthesis, Catabolism, and Signaling

Our findings suggest that a cluster of low-affinity repressive binding sites evolved in concert with regulatory neofunctionalization of *RCO* to delimit its expression. However, it is not known through which target genes RCO represses growth to generate complex leaves and how *RCO* autorepression influences such RCO-dependent growth regulation. To help identify RCO target genes, we used RNA-seq in combination with hierarchical clustering to assay RCO-dependent gene expression 2–10 h after dexamethasone-induced RCO activation in the *rco* mutant at 2-h time intervals (Figures S5A and S5B). Several Gene Ontology (GO) terms were enriched in RCO-responsive genes that relate to response to stimulus and hormones, including cytokinin (CK), and to hormone-mediated signaling (Data S1C–S1E). For example, *RCO* induction was accompanied by increased expression of *LONELY GUY 7*

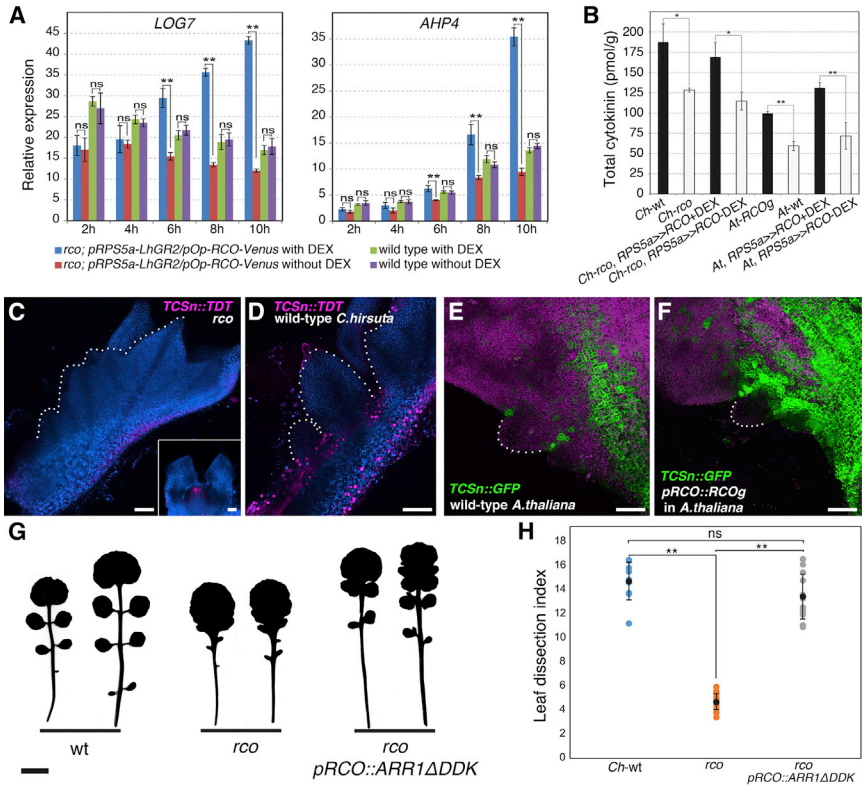

Figure 4. Cytokinin Mediates RCO Function

(A) Bar plots showing expression levels of RCO target genes as measured by qRT-PCR at different time intervals of dexamethasone-induced *RCO* expression, relative to a *UBQ10* standard. Values show mean qRT-PCR measurements of three biological replicates. Error bars represent ± 1 SD.

(B) A bar plot showing quantification of total cytokinin levels in *C. hirsuta* WT, *rco*, *A. thaliana ChRCOg*, *A. thaliana* WT, and DEX-inducible RCO lines with (+DEX) or without (−DEX) dexamethasone. Error bars represent ± 1 SD.

(C and D) Confocal projections showing the expression of *TCSn::TDT* (magenta) and chlorophyll autofluorescence (blue) in the leaves of *C. hirsuta rco* (C) and WT (D). Inset in (C) shows the signal detectable in the apex (n = 5).

(E and F) Magnified views of leaflets showing *TCSn::GFP* expression (green) and chlorophyll autofluorescence (magenta) in *A. thaliana* WT (E) and *A. thaliana pRCO::RCOg* (F; n = 5). Leaf/leaflet margins are marked by dotted outlines. Note an increased and broader expression of *TCSn::GFP* in *Arabidopsis* plants expressing *pRCO::RCOg* (compare F with E).

(G) Silhouettes of leaves 5 to 6 from *C. hirsuta* WT, *rco*, and *rco* expressing *pRCO:: ARR1ΔDDK*. Note the emergence of better separated leaflets in the *rco* mutant leaves expressing *pRCO:: ARR1ΔDDK*, indicating that increased cytokinin activity within the RCO domain could partially bypass the requirement of RCO action to promote leaf complexity.

(H) Leaf dissection index of WT *C. hirsuta*, *rco* mutants, and in *rco* mutant lines harboring *pRCO::ARR1ΔDDK*. Error bars indicate ± 1 SD based on at least 10 independent lines. A two-tailed Student's t test was used to calculate the significance in (A), (B) and (H): *p < 0.05; **p < 0.01; ns, not significant. Scale bars, 50 μm (C–F) and 1 cm (G).

See also Figures S5 and S6 and Data S1C.

(*LOG7*) and *HISTIDINE-CONTAINING PHOSPHOTRANSFER FACTOR 4* (*AHP4*) genes, which are involved in CK biosynthesis and signaling, respectively [28]. Additionally, several *CYTOKININ OXIDASE* genes had reduced expression after *RCO* induction (such as *CKX2*, *CKX3*, and *CKX6*), as well as the *URIDINE DIPHOSPHATE GLYCOSYLTRANSFERASE* (*UGT85A1*) (Data S1C), which are involved in CK degradation and inactivation [28, 29]. GO analysis of the ChIP-seq data also showed a significant enrichment for hormonal response terms, including response to CK (Data S1F). These findings suggest that RCO might act via the CK pathway.

To identify CK-related genes that are direct targets of RCO, we compared differentially expressed genes in the ChIP-seq and RNA-seq datasets and found 31 overlapping genes (Figure S5C). A Fisher's exact test confirmed that this number of overlapping genes is significantly higher than expected by chance ($p < 0.005$). *LOG7* and *AHP4* are included in these overlapping genes, and our ChIP results show that RCO associates with the promoter of these genes (Figure S5D; Table S1). Interestingly, *LOG7* and *AHP4* respond similarly to *RCO* and both are classified in cluster I (Figure S5B) and show continuously increasing expression upon *RCO* induction (Figure 4A). In contrast to *LOG7* and *AHP4*, *CKX3* is classified in cluster VIII and continuously decreases in expression upon *RCO* induction (Figure S5B). Taken together, these results suggest that RCO might enhance cytokinin biosynthesis and/or signaling. To test this hypothesis, we measured endogenous CK levels in wild-type *C. hirsuta*, the *rco* mutant, wild-type *A. thaliana*, *ChRCOg*-expressing *A. thaliana*, and in transgenic *C. hirsuta rco* mutant and *A. thaliana* expressing DEX-inducible RCO (*pRPS5a>>RCO*). The presence or induction of the *RCO* gene increased endogenous CK levels (Figures 4B and S6A). We also used the CK-response markers *TCSn::TDT* and *TCSn::GFP* (TCS) [30] to examine CK signaling activity in wild-type *C. hirsuta*, the *rco* mutant, *ChRCOg*-expressing *A. thaliana*, and wild-type *A. thaliana*, which lacks the *RCO* gene (Figures 4C–4F). In agreement with the above results, we found that presence of the *RCO* gene leads to increased *TCS* expression in leaves, especially adjacent to leaflet primordia (*C. hirsuta*) or serrations (*A. thaliana*), indicating higher CK activity. We also found that higher *RCO* expression levels, caused by mutation of RCO-binding sites, resulted in increased *LOG7*, *AHP4*, and *ARR5* expression (Figure S6B). Together, these results indicate that RCO promotes CK activity and that RCO autorepression attenuates this function.

Genetically Elevating CK Activity in the RCO Domain Is Sufficient to Promote Leaf Complexity and Partially Bypass the Requirement for RCO in Leaf Development

Based on these results, we hypothesized that RCO increased leaf complexity by stimulating CK activity at the flanks of developing leaflets, thus contributing to their separation. If RCO is

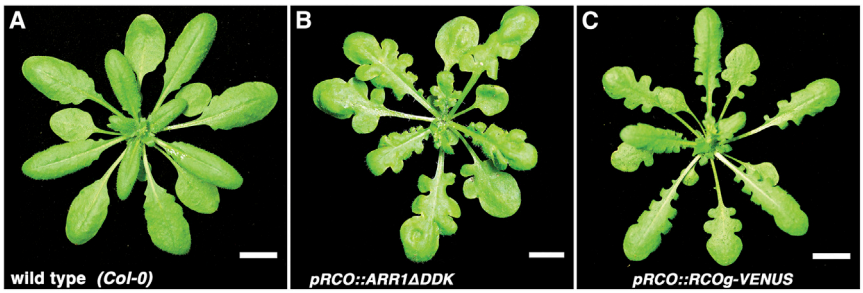

Figure 5. Increased CK Signaling Mimics the Action of RCO in Promoting *Arabidopsis* Leaf Complexity

Rosette leaves of *A. thaliana* WT plants (A), *Arabidopsis* plants expressing *pRCO::ARR1ΔDDK* (J) (n = 10 T1 lines; B), and *pRCO::RCOg-VENUS* (C). Note the increased complexity in the leaves of *Arabidopsis* plants expressing *pRCO::ARR1ΔDDK*, resembling the effects of *RCO* (compare B and C). Scale bars, 1 cm (A–C).

required for local CK activity, and if the reduced complexity of leaves in the *rco* mutant reflects decreased CK activity, we should be able to partially bypass the requirement of RCO for leaflet separation by activating CK signaling in the RCO domain. To test this idea, we enhanced CK signaling by expressing *ARR1ΔDDK*, a constitutively active form of the type-B cytokinin response regulator ARR1 [31], from the *RCO* promoter in the *rco* mutant. Consistent with our hypothesis, this transgene suppressed the *rco* mutant leaf phenotype, making it more similar, although not identical, to wild type (Figures 4G and 4H). In addition, the expression of *pRCO::ARR1ΔDDK* in *A. thaliana* converted simple *A. thaliana* leaves into complex ones, mimicking the effect of expressing *RCOg* in *A. thaliana* (Figures 5A–5C) and indicating that locally elevated CK signaling in the RCO domain is sufficient to dramatically increase complexity in *A. thaliana* leaves.

We next investigated whether similar cell-level effects underlie the increased leaf complexity caused by elevating either CK signaling or expressing RCO in the RCO domain in *A. thaliana* leaves, which should be the case if CK mediates RCO function (Figures 5 and 6). Consistent with this idea, we observed that both cell area and cell lobeyness—a differentiation measure—are reduced to a similar level relative to wild-type in *pRCO::ARR1ΔDDK* and *pRCO::RCOg-VENUS* expressing plants (Figures 6A–6D). These observations indicate that the repressive effect of RCO and CK on local leaf growth involves

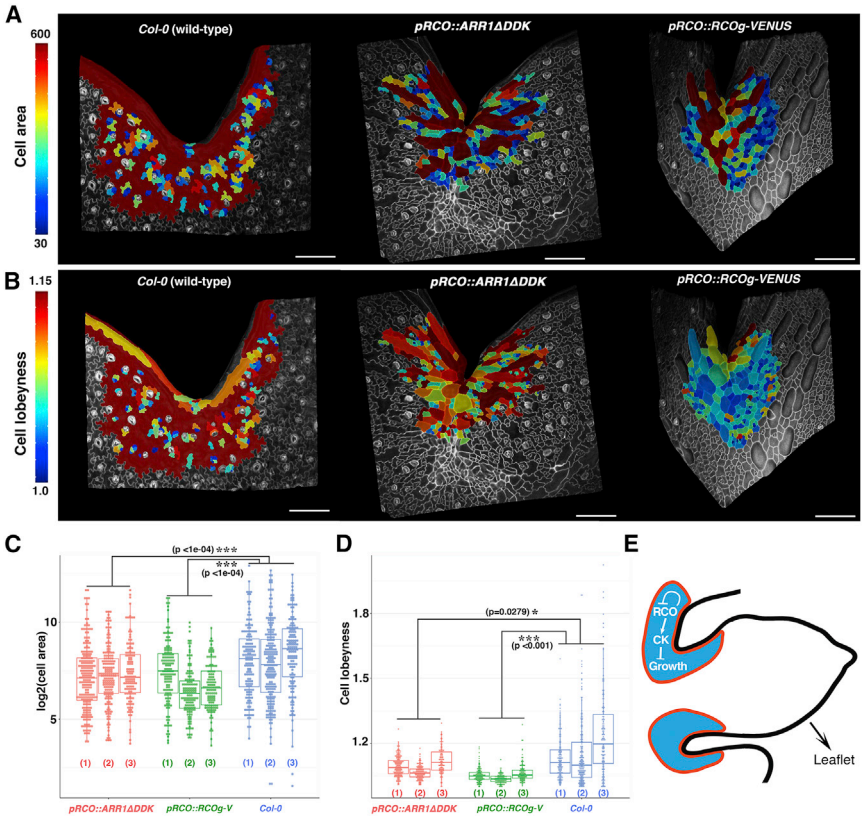

Figure 6. Increased CK Signaling in the RCO Domain Reduces Cell Size and Delays Cell Differentiation

(A) Heatmaps of quantification of cell area in the sinuses of *Arabidopsis* WT plants and *Arabidopsis* plants transformed with *pRCO::ARR1ΔDDK* and *pRCO::RCOg-VENUS*.

(B) Heatmaps of quantification of cell lobeyness—a feature that leaf epidermal cells acquire when they differentiate—in the sinuses of *Arabidopsis* WT plants and *Arabidopsis* plants transformed with *pRCO::ARR1ΔDDK* and *pRCO::RCOg-VENUS*. Scale bars, 100 μm (A and B).

(C and D) Quantifications of cell area (C) and cell lobeyness (D) in *Arabidopsis* plants transformed with *pRCO::ARR1ΔDDK* and *pRCO::RCOg-VENUS* relative to WT plants (three biological replicates each). Note the average cell area and lobeyness in both transgenic lines are significantly reduced compared to WT. The measurements and statistical analysis were restricted to all cells with a neighborhood of 5 cells centered on a focal cell at the center of the sinuses in between the lobes (also see STAR Methods). For statistical validation, two independent nested ANOVAs with genotype as a fixed factor and replicates as nested random factor were used. Significance of all pairwise comparisons between genotypes was performed using Tukey's all-pair comparison. Cell area: $p < 1e{-}04$ (WT versus *pRCO::ARR1ΔDDK*); $p < 1e{-}04$ (WT versus *pRCO::RCOg-VENUS*). Cell lobeyness: $p = 0.0279$ (WT versus *pRCO::ARR1ΔDDK*); $p < 0.001$ (WT versus *pRCO::RCOg-VENUS*).

(E) A conceptual diagram summarizing RCO function and its mechanism of action at the base of developing leaflets.

reduced cell size and is associated with slowing down differentiation. These findings are also in line with observations that increased cytokinin levels can cause a reduction in leaf cell size [32, 33]. In conclusion, RCO regulates leaf shape, at least in part, by reprogramming local CK homeostasis, thereby reducing cell growth (Figure 6E).

Finally, we asked whether the large effects of the RCO/CK module on leaf form are mirrored by large effects on the transcriptome that distinguishes *A. thaliana* and *C. hirsuta* leaves. An alternative would be that this module alters morphology via more restricted effects on this evolutionary divergent transcriptome. We found that RCO-responsive genes, including CK-related ones, are strongly overrepresented in the transcriptome that is differentially expressed between *A. thaliana* and *C. hirsuta* leaf primordia [34] (Data S1G and S1H), supporting the above "large effect on both transcriptome and morphology" hypothesis. Taken together, our findings suggest that the effect of RCO in leaf shape evolution likely reflects the integration of two opposing processes: the first creates the possibility for morphological change through re-shaping the developing leaf transcriptome and CK response, and the second limits the potentially pleiotropic effects of RCO by negative autoregulation via low-affinity binding sites. It is of note that this regulatory logic is in line with RCO acting both as an activator (e.g., of CK-related genes) and a repressor of its own transcription. This dual action may have put it in a favored position for contributing to evolutionary change by allowing fine-grained control of organ development. In the future, it will be interesting to explore the precise significance of RCO autoregulation for CK-dependent cell growth control. For example, from a theoretical perspective, negative autoregulation can reduce the effects of noise on genetic network readouts, so it is possible that this RCO/CK regulatory module allows tighter control of growth during leaf primordium development [35, 36]. CK is also important for leaf complexity in tomato [37], where leaflets evolved without a contribution of RCO [18]. It will thus be interesting to determine which genes fulfill a role similar to RCO to locally regulate CK in that system. It will also be important to understand how RCO effects on CK are integrated with those of KNOX proteins [16, 20]. These transcription factors also promote leaf complexity in a CK-related pathway that appears distinct from RCO [16, 38] as it has much broader effects on leaf primordium growth [20]. CK effects on leaf cell development are multifaceted and include modulation of the rate of cell proliferation, the timing of its cessation, as well as regulation of post-mitotic growth [33, 39]. Consequently, answering this question will require cell-level dissection of CK pathways at different developmental stages.

Conclusions

Previous studies demonstrated that low-affinity transcription factor binding sites play a crucial role in activating developmental genes, thereby ensuring developmental robustness and precise patterns of tissue development [14, 40, 41]. Here, using plant leaves and regulation of CK homeostasis as an example, we show that low-affinity repressive binding sites played a major role in the generation of morphological diversity. Specifically, our work indicates that these sites can help resolve conflicts between pleiotropy and novelty that emerge during evolution by dampening the effects of *cis*-regulatory changes that underlie novel gene expression patterns [1, 9, 15].

STAR★METHODS

Detailed methods are provided in the online version of this paper and include the following:

- KEY RESOURCES TABLE
- LEAD CONTACT AND MATERIALS AVAILABILITY
- EXPERIMENTAL MODEL AND SUBJECT DETAILS
  - Plant Growth conditions
- METHOD DETAILS
  - Construction of binary and bacterial expression vectors
  - Agrobacterium-mediated Transformation
  - Cytokinin reporter constructs and lines
  - Quantitative RT-PCR
  - Purification of RCO Protein Expressed in *Escherichia coli*
  - Protein binding microarray assay
  - EMSA
  - β -Glucuronidase (GUS) staining
  - Confocal microscopy
  - Leaf shape analysis
  - Cellular measurements
  - Dexamethasone treatment
  - Transcriptome sequence data analysis
  - ChIP-Seq
  - ChIP-Seq data analysis
  - Calculating the probability of observing zero high-affinity binding sites at the RCO locus under a neutral evolutionary model
  - Cytokinin analysis by LC-MS/MS
  - Statistical Analysis
  - GO analysis
- DATA AND CODE AVAILABILITY

SUPPLEMENTAL INFORMATION

Supplemental Information can be found online at https://doi.org/10.1016/j.cub.2019.10.040.

ACKNOWLEDGMENTS

We thank Nicolas Gompel, George Coupland, Angela Hay, and Sheila McCormick for critical comments on the manuscript and Justin Crocker for discussions on low-affinity binding sites; the late Ian Moore for *pOpIn2* constructs; Mahdieh Alipour Kermani and Lukas Baumgarten for technical assistance; and Ismene Karakasilioti for manuscript curation. J.M.F.-Z. was supported by Spanish MINECO grant BIO2017-86651-P (AEI/FEDER); K.L. and M.K. by the Swedish Foundation for Strategic Research (VINNOVA), the Knut and Alice Wallenberg Foundation (KAW), and the Swedish Research Council (VR); and M.T. by Deutsche Forschungsgemeinschaft (SFB 680) and a core grant from the Max Planck Society. M.T. also acknowledges support of CEPLAS. We thank the Swedish Metabolomics Centre for the use of instrumentation and the Max Planck Cologne Genome Center for sequencing.

AUTHOR CONTRIBUTIONS

M.H. performed the majority of the experiments and analyses and prepared figures. M.H., F.V., Y.W., and M.T. designed experiments. F.V. and Y.W.

conducted CK-related gene expression analyses and verified data and strains. N.B. performed imaging and analysis for cellular morphology quantifications and verified strains. J.M.F.-Z. conducted PBM analyses, M.K. and K.L. conducted CK analyses, and X.G. contributed to bioinformatics analyses, particularly ChIP-seq. B.M., B.R.O., R.D.I., and A.W. contributed materials. R.A.M. contributed to RNA-seq. M.T. and M.H. co-wrote the first draft of the paper, which was refined by M.T. with input from other authors, particularly Y.W., P.H., and N.B. S.L. conducted statistical analysis and contributed to data interpretation, and P.H. contributed to data analysis and validation, particularly for imaging work and figure organization. M.T. designed and directed the study.

DECLARATION OF INTERESTS

The authors declare no competing interests.

Received: August 1, 2019
Revised: October 8, 2019
Accepted: October 21, 2019
Published: November 21, 2019

REFERENCES

1. Carroll, S.B. (2008). Evo-devo and an expanding evolutionary synthesis: a genetic theory of morphological evolution. Cell *134*, 25–36.
2. Chan, Y.F., Marks, M.E., Jones, F.C., Villarreal, G., Jr., Shapiro, M.D., Brady, S.D., Southwick, A.M., Absher, D.M., Grimwood, J., Schmutz, J., et al. (2010). Adaptive evolution of pelvic reduction in sticklebacks by recurrent deletion of a *Pitx1* enhancer. Science *327*, 302–305.
3. Frankel, N., Erezyilmaz, D.F., McGregor, A.P., Wang, S., Payre, F., and Stern, D.L. (2011). Morphological evolution caused by many subtle-effect substitutions in regulatory DNA. Nature *474*, 598–603.
4. Gompel, N., Prud'homme, B., Wittkopp, P.J., Kassner, V.A., and Carroll, S.B. (2005). Chance caught on the wing: *cis*-regulatory evolution and the origin of pigment patterns in *Drosophila*. Nature *433*, 481–487.
5. Hay, A., and Tsiantis, M. (2006). The genetic basis for differences in leaf form between *Arabidopsis thaliana* and its wild relative *Cardamine hirsuta*. Nat. Genet. *38*, 942–947.
6. Indjeian, V.B., Kingman, G.A., Jones, F.C., Guenther, C.A., Grimwood, J., Schmutz, J., Myers, R.M., and Kingsley, D.M. (2016). Evolving new skeletal traits by *cis*-regulatory changes in bone morphogenetic proteins. Cell *164*, 45–56.
7. Rast-Somssich, M.I., Broholm, S., Jenkins, H., Canales, C., Vlad, D., Kwantes, M., Bilsborough, G., Dello Ioio, R., Ewing, R.M., Laufs, P., et al. (2015). Alternate wiring of a *KNOXI* genetic network underlies differences in leaf development of *A. thaliana* and *C. hirsuta*. Genes Dev. *29*, 2391–2404.
8. Studer, A., Zhao, Q., Ross-Ibarra, J., and Doebley, J. (2011). Identification of a functional transposon insertion in the maize domestication gene *tb1*. Nat. Genet. *43*, 1160–1163.
9. Doebley, J., and Lukens, L. (1998). Transcriptional regulators and the evolution of plant form. Plant Cell *10*, 1075–1082.
10. Stern, D.L., and Orgogozo, V. (2009). Is genetic evolution predictable? Science *323*, 746–751.
11. Rebeiz, M., Patel, N.H., and Hinman, V.F. (2015). Unraveling the tangled skein: the evolution of transcriptional regulatory networks in development. Annu. Rev. Genomics Hum. Genet. *16*, 103–131.
12. Rebeiz, M., and Tsiantis, M. (2017). Enhancer evolution and the origins of morphological novelty. Curr. Opin. Genet. Dev. *45*, 115–123.
13. Preger-Ben Noon, E., Davis, F.P., and Stern, D.L. (2016). Evolved repression overcomes enhancer robustness. Dev. Cell *39*, 572–584.
14. Crocker, J., Abe, N., Rinaldi, L., McGregor, A.P., Frankel, N., Wang, S., Alsawadi, A., Valenti, P., Plaza, S., Payre, F., et al. (2015). Low affinity binding site clusters confer hox specificity and regulatory robustness. Cell *160*, 191–203.
15. Crocker, J., Noon, E.P., and Stern, D.L. (2016). The soft touch: low-affinity transcription factor binding sites in development and evolution. Curr. Top. Dev. Biol. *117*, 455–469.
16. Bar, M., and Ori, N. (2014). Leaf development and morphogenesis. Development *141*, 4219–4230.
17. Maugarny-Calès, A., and Laufs, P. (2018). Getting leaves into shape: a molecular, cellular, environmental and evolutionary view. Development *145*, dev161646.
18. Vlad, D., Kierzkowski, D., Rast, M.I., Vuolo, F., Dello Ioio, R., Galinha, C., Gan, X., Hajheidari, M., Hay, A., Smith, R.S., et al. (2014). Leaf shape evolution through duplication, regulatory diversification, and loss of a homeobox gene. Science *343*, 780–783.
19. Vuolo, F., Mentink, R.A., Hajheidari, M., Bailey, C.D., Filatov, D.A., and Tsiantis, M. (2016). Coupled enhancer and coding sequence evolution of a homeobox gene shaped leaf diversity. Genes Dev. *30*, 2370–2375.
20. Kierzkowski, D., Runions, A., Vuolo, F., Strauss, S., Lymbouridou, R., Routier-Kierzkowska, A.-L., Wilson-Sánchez, D., Jenke, H., Galinha, C., Mosca, G., et al. (2019). A growth-based framework for leaf shape development and diversity. Cell *177*, 1405–1418.e17.
21. Zhang, Y., Liu, T., Meyer, C.A., Eeckhoute, J., Johnson, D.S., Bernstein, B.E., Nusbaum, C., Myers, R.M., Brown, M., Li, W., and Liu, X.S. (2008). Model-based analysis of ChIP-seq (MACS). Genome Biol. *9*, R137.
22. Franco-Zorrilla, J.M., López-Vidriero, I., Carrasco, J.L., Godoy, M., Vera, P., and Solano, R. (2014). DNA-binding specificities of plant transcription factors and their potential to define target genes. Proc. Natl. Acad. Sci. USA *111*, 2367–2372.
23. Grant, C.E., Bailey, T.L., and Noble, W.S. (2011). FIMO: scanning for occurrences of a given motif. Bioinformatics *27*, 1017–1018.
24. Ma, W., Noble, W.S., and Bailey, T.L. (2014). Motif-based analysis of large nucleotide data sets using MEME-ChIP. Nat. Protoc. *9*, 1428–1450.
25. Barrilleaux, B.L., Burow, D., Lockwood, S.H., Yu, A., Segal, D.J., and Knoepfler, P.S. (2014). Miz-1 activates gene expression via a novel consensus DNA binding motif. PLoS ONE *9*, e101151.
26. Inukai, S., Kock, K.H., and Bulyk, M.L. (2017). Transcription factor-DNA binding: beyond binding site motifs. Curr. Opin. Genet. Dev. *43*, 110–119.
27. Slattery, M., Ma, L., Négre, N., White, K.P., and Mann, R.S. (2011). Genome-wide tissue-specific occupancy of the Hox protein Ultrabithorax and Hox cofactor Homothorax in *Drosophila*. PLoS ONE *6*, e14686.
28. Kieber, J.J., and Schaller, G.E. (2018). Cytokinin signaling in plant development. Development *145*, dev149344.
29. Schmülling, T., Werner, T., Riefler, M., Krupková, E., and Bartrina y Manns, I. (2003). Structure and function of cytokinin oxidase/dehydrogenase genes of maize, rice, *Arabidopsis* and other species. J. Plant Res. *116*, 241–252.
30. Zürcher, E., Tavor-Deslex, D., Lituiev, D., Enkerli, K., Tarr, P.T., and Müller, B. (2013). A robust and sensitive synthetic sensor to monitor the transcriptional output of the cytokinin signaling network in planta. Plant Physiol. *161*, 1066–1075.
31. Sakai, H., Honma, T., Aoyama, T., Sato, S., Kato, T., Tabata, S., and Oka, A. (2001). ARR1, a transcription factor for genes immediately responsive to cytokinins. Science *294*, 1519–1521.
32. Craft, J., Samalova, M., Baroux, C., Townley, H., Martinez, A., Jepson, I., Tsiantis, M., and Moore, I. (2005). New pOp/LhG4 vectors for stringent glucocorticoid-dependent transgene expression in *Arabidopsis*. Plant J. *41*, 899–918.
33. Skalák, J., Vercruyssen, L., Claeys, H., Hradilová, J., Černý, M., Novák, O., Plačková, L., Saiz-Fernández, I., Skaláková, P., Coppens, F., et al. (2019). Multifaceted activity of cytokinin in leaf development shapes its size and structure in *Arabidopsis*. Plant J. *97*, 805–824.
34. Gan, X., Hay, A., Kwantes, M., Haberer, G., Hallab, A., Ioio, R.D., Hofhuis, H., Pieper, B., Cartolano, M., Neumann, U., et al. (2016). The *Cardamine hirsuta* genome offers insight into the evolution of morphological diversity. Nat. Plants *2*, 16167.

35. Alon, U. (2007). Network motifs: theory and experimental approaches. Nat. Rev. Genet. *8*, 450–461.
36. Crews, S.T., and Pearson, J.C. (2009). Transcriptional autoregulation in development. Curr. Biol. *19*, R241–R246.
37. Bar, M., Israeli, A., Levy, M., Ben Gera, H., Jiménez-Gómez, J.M., Kouril, S., Tarkowski, P., and Ori, N. (2016). CLAUSA is a MYB transcription factor that promotes leaf differentiation by attenuating cytokinin signaling. Plant Cell *28*, 1602–1615.
38. Jasinski, S., Piazza, P., Craft, J., Hay, A., Woolley, L., Rieu, I., Phillips, A., Hedden, P., and Tsiantis, M. (2005). KNOX action in *Arabidopsis* is mediated by coordinate regulation of cytokinin and gibberellin activities. Curr. Biol. *15*, 1560–1565.
39. Hay, A., and Tsiantis, M. (2010). KNOX genes: versatile regulators of plant development and diversity. Development *137*, 3153–3165.
40. Gaudet, J., and Mango, S.E. (2002). Regulation of organogenesis by the Caenorhabditis elegans FoxA protein PHA-4. Science *295*, 821–825.
41. Farley, E.K., Olson, K.M., Zhang, W., Brandt, A.J., Rokhsar, D.S., and Levine, M.S. (2015). Suboptimization of developmental enhancers. Science *350*, 325–328.
42. Wielopolska, A., Townley, H., Moore, I., Waterhouse, P., and Helliwell, C. (2005). A high-throughput inducible RNAi vector for plants. Plant Biotechnol. J. *3*, 583–590.
43. Hajheidari, M., Farrona, S., Huettel, B., Koncz, Z., and Koncz, C. (2012). CDKF;1 and CDKD protein kinases regulate phosphorylation of serine residues in the C-terminal domain of *Arabidopsis* RNA polymerase II. Plant Cell *24*, 1626–1642.
44. Berger, M.F., and Bulyk, M.L. (2009). Universal protein-binding microarrays for the comprehensive characterization of the DNA-binding specificities of transcription factors. Nat. Protoc. *4*, 393–411.
45. McLellan, T., and Endler, J.A. (1998). The relative success of some methods for measuring and describing the shape of complex objects. Syst. Biol. *47*, 264–281.
46. Barbier de Reuille, P., Routier-Kierzkowska, A.L., Kierzkowski, D., Bassel, G.W., Schüpbach, T., Tauriello, G., Bajpai, N., Strauss, S., Weber, A., Kiss, A., et al. (2015). MorphoGraphX: a platform for quantifying morphogenesis in 4D. eLife *4*, 05864.
47. Anders, S., and Huber, W. (2010). Differential expression analysis for sequence count data. Genome Biol. *11*, R106.
48. Mott, R., Yuan, W., Kaisaki, P., Gan, X., Cleak, J., Edwards, A., Baud, A., and Flint, J. (2014). The architecture of parent-of-origin effects in mice. Cell *156*, 332–342.
49. Li, H., and Durbin, R. (2009). Fast and accurate short read alignment with Burrows-Wheeler transform. Bioinformatics *25*, 1754–1760.
50. Landt, S.G., Marinov, G.K., Kundaje, A., Kheradpour, P., Pauli, F., Batzoglou, S., Bernstein, B.E., Bickel, P., Brown, J.B., Cayting, P., et al. (2012). ChIP-seq guidelines and practices of the ENCODE and modENCODE consortia. Genome Res. *22*, 1813–1831.
51. Love, M.I., Huber, W., and Anders, S. (2014). Moderated estimation of fold change and dispersion for RNA-seq data with DESeq2. Genome Biol. *15*, 550.
52. Dobrev, P.I., and Kamínek, M. (2002). Fast and efficient separation of cytokinins from auxin and abscisic acid and their purification using mixed-mode solid-phase extraction. J. Chromatogr. A *950*, 21–29.
53. Svačinová, J., Novák, O., Plačková, L., Lenobel, R., Holík, J., Strnad, M., and Doležal, K. (2012). A new approach for cytokinin isolation from *Arabidopsis* tissues using miniaturized purification: pipette tip solid-phase extraction. Plant Methods *8*, 17.

STAR★METHODS

KEY RESOURCES TABLE

REAGENT or RESOURCE	SOURCE	IDENTIFIER
Antibodies		
GFP-Trap Magnetic Agarose affinity beads	Chromotek	Cat# gtma; RRID: AB_2631358
IgG	Diagenode	Cat# C15410206; RRID: AB_2722554
Rabbit Anti-Maltose Binding Protein antibody	abcam	Cat# ab9084; RRID: AB_306992
goat anti-rabbit IgG DyLight 550 conjugated	Thermo Fisher Scientific	Cat# 84541; RRID: AB_10942173
Chemicals, Peptides, and Recombinant Proteins		
MS basal salt mixture with vitamin	Duchefa	N/A
MES	Sigma	M2933
BAP (6-benzylamino purine)	Sigma	B3274
Silwet L77	Obermeier	7060-10
SuperScript VILO	Invitrogen	11754050
Isopropyl-β-d-thiogalactopyranoside (IPTG)	Roth	2316
Phenylmethylsulfonylfluoride (PMSF)	Sigma	P7626
Benzamidine	Roth	CN38
Aprotinin	Roth	A162
Leupeptin	Roth	CN33
Glutathione-Sepharose 4B	Amersham Biosciences	17075605
HiTrap DEAE-Sepharose FF anion exchange column	GE Healthcare	17505501
BSA	Pharmacia	27-8915-01
Coomassie Blue	Roth	3862
Denatured salmon sperm DNA (ssDNA)	Roth	5434
HEPES	BIOMOL	05288
DTT	Carl Roth	6908
Poly(dI-dC)	Thermo	20148E
IRDye 800-labeled Dann	Metabion	N/A
Novex 6% DNA retardation gels	Invitrogen	EC6365BOX
5-bromo-4-chloro-3-indolyl-β-D-glucuronic acid (X-Gluc)	Roth	0018
Dexamethasone	Sigma	D4902
DMSO	Roth	4720
Igepal	Sigma	I3021
Protease inhibitor cocktail	Sigma	P9599
Polyvinylidene fluoride membranes	Millipore	N/A
Propidium Iodide (PI)	Sigma	87-51-4
MS basal salt mixture with vitamin	Duchefa	N/A
MES	Sigma	M2933
BAP (6-benzylamino purine)	Sigma	B3274
Silwet L77	Obermeier	7060-10
SuperScript VILO	Invitrogen	11754050
Isopropyl-β-d-thiogalactopyranoside (IPTG)	Roth	2316
Phenylmethylsulfonylfluoride (PMSF)	Sigma	P7626
Benzamidine	Roth	CN38
Aprotinin	Roth	A162
Leupeptin	Roth	CN33
Propidium Iodide (PI)	Sigma-Aldrich	87-51-4

(*Continued on next page*)

Continued

REAGENT or RESOURCE	SOURCE	IDENTIFIER
Deposited Data		
ChIP-seq data ChIP-seq data have been deposited at the European Nucleotide Archive (ENA).	This study	https://www.ebi.ac.uk/ena/data/view/PRJEB29759
RNA-seq data are available at the European Nucleotide Archive (ENA)	This study	https://www.ebi.ac.uk/ena/data/view/PRJEB29757
Experimental Models: Organisms/Strains		
Cardamine hirsuta rco/ pRCO::RCOg-VENUS-RCOter	This study	N/A
Cardamine hirsuta rco /pmutRCO::RCOg-VENUS-RCOter	This study	N/A
Cardamine hirsuta rco/ pmutRCO::RCOcds-VENUS-RCOter	This study	N/A
Cardamine hirsuta rco/ pRCO::RCOcds-VENUS-RCOter	This study	N/A
Cardamine hirsuta rco/ pRCO::ARR1ΔDDK	This study	N/A
Arabidopsis/ pRCO::ARR1ΔDDK	This study	N/A
Arabidopsis/ pRCO::RCOg-VENUS-RCOter	N/A	N/A
Arabidopsis/ pRCO::RCOg- RCOter/ TCSn::GFP	This study	N/A
Arabidopsis/TCSn::GFP	[21]	N/A
Cardamine hirsuta rco/ pRCO::RCO-3HA	[19]	N/A
Cardamine hirsute rco/ pRCO::RCOA48D-3HA	[19]	N/A
Cardamine hirsuta rco/ pRCO::GUS	N/A	N/A
Cardamine hirsuta wt (ox)/pRCO::GUS	[18]	N/A
Cardamine hirsute rco/ pOpIn2 -pOp6::RCO-VENUS	This study	N/A
Cardamine hirsuta rco/ TCSn::tdTOM	This study	N/A
Cardamine hirsuta wt/ *TCSn::tdTOM*	This study	N/A
Recombinant DNA		
pRCO::RCOg-VENUS-RCOter	This study	N/A
pmutRCO::RCOg-VENUS-RCOter _	This study	N/A
pmutRCO::RCOcds-VENUS-RCOter	This study	N/A
pRCO::RCOcds-VENUS-RCOter	This study	N/A
pRCO::ARR1ΔDDK	This study	N/A
(TCSn)::tdTomato	This study	N/A
pOpIn2 -pOp6::RCO-VENUS	This study	N/A
pRCO::RCOg	This study	N/A
pmutRCO::RCOcds	This study	N/A
Software and Algorithms		
AlphaVIEW SA software v1.0.2	Cell Biosciences	N/A
ImageJ	ImageJ 1.51j8, National Institutes of Health, USA	N/A
Odyssey Infrared Imaging System (LI-COR)	N/A	N/A
MorphographX	[42]	N/A

LEAD CONTACT AND MATERIALS AVAILABILITY

Further information and requests for resources (plasmids and transgenic lines generated in this study, listed in the Key Resources Table) should be directed to and will be fulfilled by the Lead Contact, Miltos Tsiantis (tsiantis@mpipz.mpg.de).

EXPERIMENTAL MODEL AND SUBJECT DETAILS

Arabidopsis thaliana Col-0, Cardamine hirsuta Ox [5] and *Cardamine hirsuta rco* [18] backgrounds were used for experiments and for generation of transgenic lines.

Plant Growth conditions

Plant seeds were germinated and grown on soil in MPIPZ greenhouses under long day conditions (16 h of light, 8h dark) at 20 ± 2°C, with 65 ± 10% relative humidity. For dexamethasone treatment (described below), seeds were germinated and grown on half-MS-medium (Duchefa Biochem, M0222.0050 including vitamins, supplemented with 1% sucrose) containing plates in short days (8 h light: 16 h dark).

METHOD DETAILS

Construction of binary and bacterial expression vectors

To create a Dexamethasone-mediated inducible system, the *RCO-coding sequence (RCO-CDS)* fused to *VENUS* was cloned into binary vector pOPIn2-AtRPS5a-LhGR (kind gift from Ian Moore). This vector was derived from the inducible RNAi vector pOpOff2 RNAi [42] by introducing the *AtRPS5a::LhGR* cassette from a pBIN-LhGR vector [32]. It confers BASTA resistance for selection in plants. To perform ChIP-Seq, the synthesized *RCOg-VENUS* sequence fused to the *RCO* terminator was cloned immediate downstream of the *RCO* promoter in the intermediate vector pBJ36 using XmaI and *BamH*I. The whole cassette was then cloned as a *Not*I fragment into the binary vector pMLBART for plant transformation. To perform the functional analysis of RCO-binding sites, synthesized modified *RCO* promoters were transferred into the pBJ36 intermediate vector harboring either the *RCO-CDS* fused to the *RCO* terminator or the *RCO* genomic sequence fused to the *RCO* terminator using SalI and XmaI sites. Cassettes were transferred as *Not*I fragments into pMLBART for plant transformation. To understand the possible role of cytokinin signaling in the regulation of growth, the coding sequence of *ARR1ΔDDK*, (synthesized by Genscript LtD, Hong Kong), was cloned downstream of the *RCO* promoter and upstream of the *RCO* terminator in the pBJ36 intermediate vector using XmaI and BamHI sites. Cassette was transferred as *Not*I fragments into pMLBART for plant transformation. To construct a bacterial expression vector, the coding sequence of *RCO* was obtained by PCR amplification from seedling cDNAs using *RCOFBamH*I (GAACAATAAGGATCCCAAATGGAATGGTCAACCA-CAAGCAAC) and *RCO*RSalI (GAACAATAAGTCGACCTAAGGAAAAGCCTGAGATATCGCCG) oligos. The PCR product was cloned in the polylinker of the bacterial expression vector pGEX-6p-3, using *BamH*I and SalI. Finally, the construct was verified by sequencing.

Agrobacterium-mediated Transformation

C. hirsuta plants were transformed by *Agrobacterium* using the floral dip method. *Agrobacterium* cultures grown in 1000 mL YEB medium at 28°C to an OD600 of 0.8 to 1.0 were harvested by centrifugation and resuspended in infiltration medium containing 4 g/L MS basal salt mixture with vitamin (Duchefa), 3% sucrose, 10 mM $MgCl_2$, 5 mM MES pH 5.6, 0.05 μM BAP (6-benzylamino purine), and 0.05% (v/v) Silwet L77. Plant inflorescences were submerged in the *Agrobacterium* suspension for 1 minute and then covered with plastic bags for one day adaptation. Seeds were collected in nylon bags, dried and then selected.

Cytokinin reporter constructs and lines

To monitor the transcriptional output of the cytokinin network in *Arabidopsis*, *Two Component Signaling Sensor TCSn::GFP* was used [30]. To visualize this response in *C. hirsuta*, GFP was replaced with nuclear localized td-Tomato (*TCSn::tdTomato)* and the resulting construct was transformed into *C. hirsuta*.

Quantitative RT-PCR

Total RNA was extracted using the RNeasy Mini kit supplied with RNase-Free DNase (QIAGEN). Two micrograms of total RNA template were reverse-transcribed using a first-strand cDNA synthesis kit (SuperScript VILO, Invitrogen). The reaction mixture was diluted to 100 μl, and 4 to 5 μl aliquots were used for real-time PCR assays performed with iQ Supermix (Bio-Rad) in a Bio-Rad iCycler iQ5. All quantitative RT-PCR measurements were performed in triplicate from three independent experiments. The expression of *UBQ10* was used to normalize the expression of CT values. The obtained standard curves with $R^2 \geq 99$ confirmed the PCR efficiency equal to or more than 87% and equal to or less than 95% ($87 \geq E \leq 95$) for all reactions. Nonspecific amplification was examined via melting-curve analysis of the qPCR products [43]. Oligos used for quantitative RT-PCR measurements are provided in in Table S2 (related to STAR Methods).

Purification of RCO Protein Expressed in *Escherichia coli*

E. coli BL21 (DE3) pLysS cells carrying pGEX-RCO were grown at 28°C to OD_{600} of 0.4 to 0.6. Expression of the GST-RCO protein was induced by 1 mM isopropyl-β-d-thiogalactopyranoside for 4 h at 37°C. Cells were harvested by centrifugation and then resuspended and sonicated in lysis buffer (50 mM NaH_2PO_4, 300 mM NaCl, 1 mM phenylmethylsulfonylfluoride, 0.1 mM benzamidine, 10 μg/mL aprotinin, and 10 μg/mL leupeptin, pH 8.0). The cell lysate was centrifuged (Sorvall HB-4 rotor; 16,500*g* for 30 min at 4°C), and the cleared extract used for affinity purification on glutathione-Sepharose 4B (Amersham Biosciences). The eluted GST-RCO protein fraction was further purified by anion-exchange chromatography on a 1 mL pre-packed HiTrap DEAE-Sepharose FF anion exchange column (GE Healthcare). Finally, protein concentrations were adjusted based on Bradford assays (Bio-Rad) using a BSA standard curve and then confirmed by SDS/PAGE and Coomassie Blue analysis.

Protein binding microarray assay

The coding sequence of RCO was recombined in a Gateway LR reaction into pDEST-TH1 vector, yielding a translational fusion with maltose binding protein (MBP). The resulting plasmid was introduced into the BL21 strain of *E. coli* and the recombinant protein expressed as indicated above. DNA-binding assays were performed as follows [22]. An oligonucleotide nPBM11 array containing all the possible 11 bp sequences, was synthetized by Agilent Technologies. A soluble protein extract was obtained from a bacterial pellet corresponding to 25 mL of an induced culture by resuspending in 1 mL binding buffer (10 mM Tris-HCl pH 8, 60 mM KCl, 4 mM $MgCl_2$, 0.1 mM EDTA pH 8, 10% glycerol, 0.2% NP40, 200 mg/mL, 1mM Phenylmethanesulfonyl fluoride), then sonicated twice for 30 s, and centrifuged twice at 20,000 g to obtain cleared extracts. The binding mixture was adjusted to 175 μL containing 2% milk and 0.89 μg of denatured salmon sperm DNA. In parallel, the PBM array was converted to double-strand by subjecting it to a primer extension reaction containing at 1.17 μM oligonucleotide 5′-ACAGCACGGACAACGGAACACAGAC-3′, 163 μM dNTPs, 1.63 μM Cy3-dUTP (GE Healthcare PA55022), 1x Thermo Sequenase Buffer and 40 U Thermo Sequenase DNA Polymerase (GE Healthcare E79000Y). This mixture was applied to the pre-heated array and incubated for 10 min at 85°C, 10 min at 75°C, 10 min at 65°C and 90 min at 60°C. After the incubation, the slide was washed in phosphate-buffered saline (PBS), 0.01% Triton X-100 at 37°C for 10 min, followed by three washes in PBS at room temperature. The double-stranded PBM was incubated for 2.5 hours at room temperature with the protein-containing binding mixture to allow DNA-protein interactions and washed 5 times, 3 min in PBS-1% Tween 20 and 3x 5 min in PBS-0.01% Triton X-100. DNA–protein complexes were detected with sequential incubations with primary rabbit polyclonal antibody to MBP (Abcam ab9084) for 16 hours at room temperature and goat anti-rabbit IgG DyLight 550 conjugated (Thermo Fisher Scientific, 84541) in PBS–2% milk for 3 h at room temperature. After each antibody incubation, the slide was washed 3x 5 min PBS-0.05% Tween 20 and 3x 5 min PBS-0.01% Triton X-100. Finally, the array was scanned in a DNA Microarray Scanner at 2 μm resolution and quantified with Feature Extraction 9.0 software (Agilent Technologies). Normalization of probe intensities and calculation of E- and Z-scores of all the possible 8-mers were carried out with the PBM Analysis Suite [44] (also see Data S1B).

EMSA

Electrophoretic Mobility Shift Assays (EMSAs) were performed using 20-160 ng of purified GST-RCO fusion protein incubated in binding buffer [25 mM HEPES pH 7.8, 50 mM KCl, 5 mM MgCl2, 10% glycerol, 1 μg/μl BSA, 1 mM DTT, 1 mM EDTA, 0.05 μg/μl Poly(dI-dC)], and 100 fmol IRDye 800-labeled DNA] for 45 min at room temperature and subsequently loaded onto Invitrogen Novex 6% DNA retardation gels. Samples were run for 1 h at 120 V at 4°C. The gels were directly visualized using Odyssey Infrared Imaging System (LI-COR). Oligos used for these assays are provided in Table S3 (related to STAR Methods).

β -Glucuronidase (GUS) staining

GUS activity staining assays were performed as previously described [5]. Plants after fixation in 90% acetone were incubated overnight at 37°C with 1 mg/ml of 5-bromo-4-chloro-3-indolyl-β-D-glucuronic acid (X-gluc, Roth), supplemented with 2 mM ferricyanide and ferrocyanide salts. Signals were documented using a Zeiss Axiophot light microscope and Zeiss Axiocam.

Confocal microscopy

Confocal imaging was performed using a Leica SP8 microscope with 20x (HCX APO, numerical aperture 0.8). Excitation was achieved using an argon laser with 514 nm. Fluorescent signal was collected from 519 to 550 nm emission spectrum for VENUS and a 657 to 743 nm filter for the chlorophyll autofluorescence. To preserve the transgene signal against the auto-fluorescent background, it was subtracted from the auto-fluorescent background before merging both in different color channels for visual display.

Leaf shape analysis

All phenotypic measurements were performed using at least 20 independent T1 lines grown under the same conditions. To obtain leaf silhouettes, leaf 5 samples were flattened onto white paper using a clear adhesive and then digitally scanned. Leaf area and perimeter were calculated from silhouettes using ImageJ software (ImageJ 1.51j8, National Institutes of Health, USA). Leaf dissection index was then determined by using the formula [(perimeter squared)/(4π x area)] [45].

Cellular measurements

Leaf 9 of 19-days old wild-type *Arabidopsis* plants and *Arabidopsis* plants transformed with *pRCO::ARR1ΔDDK* and *pRCO::RCOg-VENUS,* grown in long day conditions (16h light, 8 hour dark) on MS medium (1% sucrose, 1X Murashige and Skoog basal salt mixture(Sigma, M5524), 0.05% MES 2-(MN-morpholino)-ethane sulfonic acid, 0.8% Bacto Agar, 1% MS vitamins (Sigma, M3900), pH 5.7 adjusted with 1M KOH) were used for analysis. Three biological replicates (leaf 9 from 3 independent plants at same stage for each genotype) were used. Leaves were dissected off the main plant body and stained with Propidium iodide (1mg/ml solution in water) for 60 minutes. Cells in the sinus regions in between the lobes 1 and 2 or serrations 1and 2 from the proximal end of the leaf were then imaged on a Leica TCS-SP8 upright confocal microscope. To detect fluorescence signal from the cell walls, PI-stained leaves were excited with 561nm white light laser and signal was collected from 565 nm to 580nm. Z stacks were acquired using HyD detectors and a 20x NA 0.8 objective in a 1024x1024 scan format with a step size of 1 μm. Leaves from all the three genotypes were imaged with the same magnification. Quantitative analysis of cell area and cell lobeyness was performed using MorphographX [20, 46]. Briefly, to extract the cell shapes, confocal stacks were loaded into MorphographX and processed to create a mesh with subsequently the signal projected onto it. Cells in the sinus regions in between the lobes or serrations were

manually segmented. For measurements shown in Figures 6C and 6D, cells within 5 cell distances from the center of the notches were included in the analysis. Cell area and cell lobeyness were calculated using the MorphographX pluggins as described previously [20]. Matured stomata cells were excluded from the analysis. For statistical validation, two independent nested ANOVA with genotype as a fixed factor and replicates as nested random factor were used. Significance of all pairwise comparisons between genotypes was performed using Tukeys all-pair comparison. We found that significance levels for difference in cell area and cell lobeyness did not change upto measurements performed on 7-cell distance from the center of the sinus in between the lobes. The R script implementing the statistical analyses and the data for individual biological replicates can be found at https://gitlab.mpcdf.mpg.de/slaurent/statistical_analyses_for_hajheidari_et_al.

Dexamethasone treatment

Fourteen-day old *rco* mutant seedlings harboring a Dexamethasone (DEX)-inducible RCO construct (*pOpIn2 -pOp6::RCO-VENUS*) were grown on MS plates in short days (8 h light: 16 h dark) and incubated in liquid MS medium with either 0.1% DMSO or 10 μM DEX. Seedlings were harvested at multiple two-hour interval time-points (2, 4, 6, 8, and 10 h) by flash freezing in liquid nitrogen. RNA samples were extracted and sequenced using the HiSeq 2500 sequencing system (Illumina). For each time point, comparative analysis was done between DEX- and DMSO-treated samples. DEX-responsive genes were identified by comparative RNA-Seq analysis between DEX- and DMSO-treated wild-type samples treated as above and excluded from downstream analyses.

Transcriptome sequence data analysis

RNA for RNA-Seq experiments was obtained from three biological replicates, and total RNA was isolated by using an RNeasy Plant Mini Kit (QIAGEN) and subsequently digested with RNase-free DNase, according to the manufacturer's protocol. A total of 1 μg of RNA was used for library preparation using TruSeq RNA Sample Preparation Kit v2 RS-122-2002 (Illumina). Library quality was validated using 2100 Bioanalyzer (Agilent), and libraries then underwent single-end sequencing (100 bp reads) using the Illumina HiSeq2500 Sequencing System. Reads were aligned to the *C. hirsuta* reference genome (CHIV1, http://chi.mpipz.mpg.de/) using STAR v2.4.2a with default parameters. Raw read counts per gene were quantified with HTSeq v0.5.4p1 (https://www-huber.embl.de/users/anders/HTSeq/) using the "–stranded=no–type=CDS" option. Differential expression was determined using DESeq2 v1.10.1 [47]. We found the most sensitive parameter settings for the function estimateDispersions were method = "blind," and sharingMode = "fit-only" [48]. RNA-Seq data are available at the European Nucleotide Archive (ENA, https://www.ebi.ac.uk/ena/data/view/PRJEB29757). (Also see Data S1C, S1D, S1G, and S1H)

ChIP-Seq

Chromatin immunoprecipitations were performed, as in [43] with some modifications. Fourteen-day old seedlings grown on soil were cross-linked with 1% formaldehyde at 4°C for 20 min, then ground with liquid nitrogen. 5-6 g homogenized tissue was resuspended in 45 mL of Nuclei isolation buffer (50 mM HEPES pH 7.4, 25 mM NaCl, 5 mM $MgCl_2$, 5% sucrose, 30% glycerol, 0.25% Triton X-100, 0.1% β-mercaptoethanol, and 0.1% protease inhibitor cocktail Sigma P9599) and centrifuged at 1600 g for 20 min at 4°C. The pellet was resuspended and washed in Nuclei washing buffer (17 mM HEPES (pH 7.4), 7 mM $MgCl_2$, 33 mM NaCl, 13% sucrose, 13% glycerol, 0.25% Triton X-100, 0.1% β-mercaptoethanol, and 0.1% protease inhibitor cocktail) three times. After centrifugation at 1600 g for 10 min, the pellet was resuspended in 500 μL of TE buffer pH = 8.0 supplemented with 1% SDS and mixed on a rotator for 60 min. The DNA was sheared by sonication in a Bioruptor (Diagenode) to 300-500 bp fragments. The chromatin solution, carrying the same amount of DNA for different samples, was diluted by IP buffer (10 mM Tris pH = 7.5, 0.5 mM EDTA, 150 mM NaCl) and incubated with GFP-Trap magnetic beads (Chromotek) or IgG coated magnetic beads. After overnight incubation with rotation at 4°C, the samples were cleared on a magnetic stand. The magnetic beads were then washed 4x2 times with washing buffers in the order as follows. Wash buffer 1: 0.1% SDS, 1% Triton-X, 2mM EDTA, 20 mM Tris-HCl pH 7.5, 150 mM NaCl. Wash buffer 2: 0.1% SDS, 1% Triton-X, 2mM EDTA, 20 mM Tris-HCl pH 7.5, 500 mM NaCl. Wash buffer 3: 0.25 M LiCl, 1% IGEPAL-CA630, 1% deoxycholate, 1mM EDTA, 10 mM Tris-HCl pH 7.5. Wash buffer 4: 10 mM Tris pH 7.5, 0.5 mM EDTA. Immunocomplexes were then eluted from the beads with 500 μL of elution buffer (50 mM Tris pH = 8.0, 10 mM EDTA, 1% SDS). Cross-linking was reversed by incubation at 37°C in the presence of 25 μg/mL proteinase K followed by at least 8 h of incubation at 65°C. The DNA was purified by two successive phenol/TE and phenol/chloroform/iso-amylalcohol extractions and ethanol-precipitated overnight at −20°C. The pellet was washed with 70% ethanol and resuspended in 30 μL of H_2O. A similar amount of untreated sonicated chromatin was phenol/chloroform purified, precipitated with ethanol overnight and resuspended in 30 μl of H_2O and used as total input DNA sample. To ensure experimental reproducibility, three biological replicates of template, mock control, and input were sequenced to a depth of 22-24 million reads. ChIP-Seq data have been deposited at the European Nucleotide Archive (ENA, https://www.ebi.ac.uk/ena/data/view/PRJEB29759).

ChIP-Seq data analysis

Illumina short reads were mapped to the reference genome using BWA version 0.7.15-r1140 with WA-MEM algorithm (command mem) with option "-M" [49]. Reads with mapping quality MAPQ < 30 or those identified as PCR duplicates by PICARD (command Markduplicates) were excluded from subsequent analyses. Stringent QC were performed using ENCODE (phase III) transcription

factor and histone ChIP-Seq pipeline specifications (by Anshul Kundaje) in https://docs.google.com/document/d/1lG_Rd7fnYgRpSIqrIfuVlAz2dW1VaSQThzk836Db99c/edit# to access the reproducibility among biological replicates [50], with MACS2 version 2.1.0.20150420 [21] selected as peak caller and P value cutoff of 1e-3.

To make sure both broad peaks and narrow peaks are detected, we followed the principle of DiffBind with minor revisions to enhance the performance for our plant studies. Reads from biological replicates were merged into two pools, case and control, for peak calling using MACS2 with "–nomodel -p 1e-3." As the number of peaks detected is smaller than 1,000 and negative binomial distributions-based statistics used by DESeq or edgeR could lose powers, pseudo-peaks were be generated from the 200bp promoter regions of annotated protein-coding genes that do not overlap with any detected peak for quality control and normalization. Raw read counts per peak (or pseudo-peaks if present) per sample were quantified with HTSeq v0.5.4p1 (https://www-huber.embl.de/users/anders/HTSeq/). Peaks showing differential binding between case and control were determined using DESeq [51] with the method = "blind," sharingMode = "fit-only" and P value cutoff of 0.05 [50]. (Also see Data S1A)

Calculating the probability of observing zero high-affinity binding sites at the RCO locus under a neutral evolutionary model

To test whether the absence of high-affinity binding sites for RCO at the *RCO* locus can be explained by chance alone, we simulated DNA under a neutral evolutionary model and subjected the simulated sequences to the same PWM-scoring method that has been used on the empirical data. For each simulated dataset, we calculated the number of high-affinity binding sites predicted by the PWM scoring algorithm and used this distribution to calculate the probability of observing no high-affinity binding sites. Neutral DNA simulations were done with *seq-gen v1.3.4* using the following options "*-mHKY -L 5000 -k 1*." The input tree was a simple bifurcation representing the duplication of *RCO* and *LMI1* with branch length $K_s/2$, where K_s is the synonymous divergence between *RCO* and *LMI1*. For each simulation, the ancestral DNA sequence was initialized by a random DNA sequence with the same nucleotide composition as observed within a 200kb region centered around *RCO* and *LMI1*. For every simulated DNA sequence, we ran the PWM scoring method implemented in *fimo v5.0.5* with the following option "*–thres 0.000619 –max-strand*." The threshold was set such as to identify sites with a PWM score larger than the highest PWM score observed in the real RCO regulatory region. The annotated script used for this analysis can be found here: https://gitlab.mpcdf.mpg.de/slaurent/statistical_analyses_for_hajheidari_et_al.

Cytokinin analysis by LC-MS/MS

Cytokinins and their related metabolites were extracted from seedlings with modified Bieleski buffer and consequently purified by using MCX separation cartridges (Waters) [52]. Samples were analyzed in 4 biological replicates. Stable isotope-labeled standards (Olchemim) for all measured compounds were added to samples before extraction. Mass spectrometry analysis and quantification was performed by LC-MS/MS, which consisted of the 1290 Infinity Binary LC System coupled to 6490 Triple Quad LC/MS System with Jet Stream and Dual Ion Funnel technologies (Agilent Technologies) [53]. Concentrations were then calculated using a standard isotope dilution method. All solvents used were of analytical or higher grade (Sigma Aldrich GmbH).

Statistical Analysis

As indicated in the text, statistical analyses were performed using a two-tailed unpaired Student's t tests, assuming equal variances (with NS, not significant; *$p < 0.05$; **$p < 0.01$) or, for Figures 3B, 3D, S2C–S2F, and S3E, using a one-way ANOVA followed by a Tukey's HSD test for multiple-pairwise comparisons (as implemented in the R base package).

GO analysis

Gene ontology (GO) analysis was done using agriGO with default settings (http://bioinfo.cau.edu.cn/agriGO/). (Also see Data S1E and S1F)

DATA AND CODE AVAILABILITY

The raw ChIP-Seq data have been deposited at the European Nucleotide Archive under project name PRJEB29759 (ENA: PRJEB29759) (ENA, https://www.ebi.ac.uk/ena/data/view/PRJEB29759). The raw RNA-Seq data are available at the European Nucleotide Archive under project name PRJEB29757 (ENA: PRJEB29757) (ENA, https://www.ebi.ac.uk/ena/data/view/PRJEB29757). The codes for RNA-Seq and ChIP-Seq data analysis are available upon request. The R scripts implementing all the statistical analyses and the visualization can be found at https://gitlab.mpcdf.mpg.de/slaurent/statistical_analyses_for_hajheidari_et_al. Raw data for cellular-morphology analysis in Figure 6 is available at Edmond repository (https://edmond.mpdl.mpg.de/imeji/collection/EBFSUTS1h4UmUfPq)(https://doi.org/10.17617/3.32).